

Scaling laws of the cavity enhancement for NV centers in diamond

Hanno Kaupp,^{1,2} Christian Deutsch,³ Huan-Cheng Chang,⁴
Jakob Reichel,⁵ Theodor W. Hänsch,^{1,2} and David Hunger^{1,2,*}

¹*Fakultät für Physik, Ludwig-Maximilians-Universität, Schellingstraße 4, 80799 München, Germany*

²*Max-Planck-Institut für Quantenoptik, Hans-Kopfermann-Str. 1, 85748 Garching, Germany*

³*Menlo Systems GmbH, 82152 Martinsried, Germany*

⁴*Institute of Atomic and Molecular Sciences, Academia Sinica, Taipei 106, Taiwan*

⁵*Laboratoire Kastler Brossel, ENS/UPMC-Paris 6/CNRS, 24 rue Lhomond, F-75005 Paris, France*

(Dated: July 5, 2022)

We employ a fiber-based optical microcavity with high Finesse to study the enhancement of fluorescence emission of NV centers in nanodiamonds. Harnessing the full tunability and open access of the resonator, we explicitly demonstrate the scaling laws of the Purcell enhancement by varying both the mode volume and the quality factor over a large range. While changes in the emission lifetime remain small in the regime of a broadband emitter, we observe an ideal Purcell factor of up to 450. Our results show a way for the realization of wavelength-tunable, narrow-band single-photon sources and demonstrate a system that has the potential to reach the strong coupling regime.

PACS numbers: 42.50.Pq, 42.50.Ct, 42.81.Qb, 61.72.jn, 81.05.ug

The negatively charged nitrogen vacancy center (NV) in diamond stands out due to stable single photon emission [1, 2] and exceptional spin coherence of electronic ground state levels [3]. Together with spin-selective optical transitions, the NV center represents a particularly promising solid state quantum bit with direct optical access [1, 3, 4]. An important milestone yet to achieve is the realization of an efficient optical interface for this emitter. Ideally it would open the way for deterministic single photon sources [5], non-destructive spin state detection [6, 7], efficient spin-photon entanglement [8], and quantum coherent optical manipulation on the single photon level. A variety of optical microcavities has been studied in this respect, including photonic crystal cavities [9–13], microring resonators [14, 15], microdiscs [16, 17], Fabry-Perot cavities [18], and plasmonic nanoresonators [19, 20]. Considerable success has already been achieved, e.g. by demonstrating Purcell enhancement of the zero phonon line (ZPL) at cryogenic temperature, where 70% of the emission was channeled into a single cavity mode [14]. The broad emission spectrum and the small weight of the ZPL call for particularly large Purcell factors to achieve efficient cavity coupling. Furthermore, several issues remain problematic for the techniques used so far, which all rely on solid state cavities with limited flexibility to access the cavity mode and to tune the resonance frequency.

In this work we study the cavity enhancement of the phonon sideband emission of small ensembles of NV centers in individual nanodiamonds by means of a fiber based Fabry-Perot microcavity [21]. The cavity design relies on concave surface profiles machined on the end faces of optical fibers using CO₂ laser processing [22]. The technique provides excellent surface quality to support ultra-low loss mirror coatings, and offers microscopic

cavity mode volumes to achieve large Purcell factors. The open resonator geometry permits to easily access the cavity field maximum, to study various emitters with one and the same cavity, and to fully tune the cavity resonance. These features have been beneficial for recent experiments with ultracold atoms [23], trapped ions [24], molecules [25], quantum dots [26–29], and NV centers in diamond [30]. Here we use these properties to explicitly demonstrate the scaling of the fluorescence enhancement for NV centers with the cavity parameters. Using direct comparison of free space and cavity enhanced emission, we determine the ideal and effective Purcell factors as a function of the mode volume and the quality factor. While narrow cavity resonances couple only to a small fraction of the broad emission spectrum, we observe an up to 450-fold enhancement of the emission spectral density, giving a direct measure of the ideal Purcell factor of the coupled system. Furthermore, we find that we can maintain a cavity Finesse $\mathcal{F} = 30000$ in the presence of rather large nanocrystals.

Setup. In our experiments we use a cavity which consists of a mirror on a concave end face of a single mode fiber and a macroscopic plane mirror, schematically shown in Fig. 1(b). The effective radius of curvature in the center of the profile machined on the fiber is $r = 100 \mu\text{m}$. Together, the two mirrors define a fully accessible microscopic cavity with a mode waist $w_0 = 2.2 \mu\text{m}$ and an effective cavity length as small as $d_{\text{eff}} = 4.3 \mu\text{m}$, which includes the penetration of the cavity mode into the dielectric mirrors. The smallest mode volume we currently achieve in this way is $V = 16 \mu\text{m}^3$. The coatings are designed for highest reflectivity at 780 nm and are realized by multiple layer pairs of Ta₂O₅ and SiO₂. At the center wavelength, the Finesse reaches a value of $F = 30000$ for small cavity

length. It decreases continuously towards $\mathcal{F} = 20000$ at $d_{\text{eff}} = 39 \mu\text{m}$ and drops faster for larger distances, which we attribute to diffraction loss due to the finite mirror size. The largest quality factor we thus obtain is $Q_0 = 2 \times 10^6$ for $d_{\text{eff}} = 39 \mu\text{m}$.

We introduce nanodiamonds containing NV centers into the cavity by directly spin coating an aqueous colloidal solution on the large mirror with low enough concentration ($< 0.01 \mu\text{m}^{-2}$) to isolate single nanocrystals with the cavity mode. For optimal coupling between the emitter and the cavity, the mirror is terminated with a $\lambda/4$ layer of SiO_2 to shift the electric field maximum of the cavity mode slightly above the mirror surface. We employ fluorescent nanodiamonds (FNDs) of 12 nm and 100 nm size which were irradiated with He ions to increase the concentration of NV centers [31, 32]. Surface treatment with acids and thermal oxygen etching removes graphitic surface shells and other contaminants. The resulting surfaces are predominantly oxygen terminated, which favors the negative charge state of the NV center [33, 34]. The emission spectrum of the NV center shows a zero phonon line at 637 nm with a room temperature linewidth of ~ 2 THz [35], and a broad phonon sideband resulting from coupling to a phonon continuum with a distinct coupling strength maximum at a phonon frequency of 16 THz [36]. Transitions involving up to ~ 6 phonons constitute the major part of the sideband fluorescence as schematically shown in Figure 1(a). Overall, the spectrum has an approximately gaussian shape with central wavelength of 685 nm and a full width at half maximum of 70 nm, see Fig. 2(a).

With our present mirror coating, the NV emission spectrum is divided into two parts: For wavelengths shorter than 690 nm, the mirrors are transmissive and the color centers emit approximately under free space conditions. For longer wavelengths, the mirrors become increasingly reflective and cavity enhanced emission can be observed. This enables us to observe free space and cavity enhanced emission within one measurement, such that the cavity enhancement can be quantified from a direct comparison. Furthermore, it strongly facilitates the search for NV centers in the cavity, since a large fraction of their emission is transmitted. High transparency at the excitation wavelength provides nearly constant excitation conditions when varying the cavity length. Finally, the strong change of mirror reflectivity across the fluorescence spectrum permits us to study the cavity enhancement as a function of the quality factor.

The cavity setup is combined with a homebuilt confocal microscope as shown in Fig. 1(c). We use an excitation laser at 532 nm (Cobolt Samba) which is coupled to a singlemode fiber and short pass filtered (Thorlabs FES0550) to remove fiber fluorescence. The light is focused with a long working distance objective (Mitutoyo, NA= 0.55) through the macroscopic mirror (diameter 0.5") onto the surface supporting the FNDs.

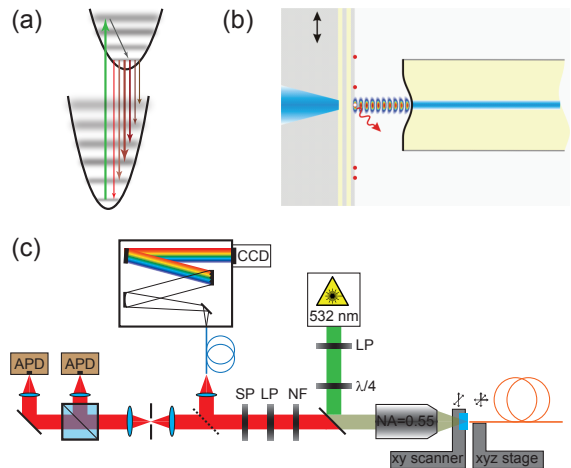


FIG. 1: (a) Level scheme of phonon assisted optical transitions in the NV optical cycle. (b) Schematic of the cavity. (c) Experimental setup combining a confocal microscope and a tunable microcavity (LP long pass, SP short pass, NF notch filter, $\lambda/4$ quarter wave plate).

The mirror is mounted on a nanopositioning stage (PI 541.2 SL) to perform raster scans and to maximize the overlap of a nanodiamond with the cavity mode. The fluorescence is collected via the same objective, separated from the excitation light with a dichroic mirror (Thorlabs DMLP567), and spectrally filtered (Thorlabs FEL0600, FES0850, NF533-17). Thereafter, the fluorescence is either spatially filtered with a pinhole and led to a Hanbury Brown-Twiss (HBT) setup with two avalanche photo diodes (Laser Components Count) behind a 50/50 beamsplitter, or coupled via a multimode fiber (Thorlabs HPSC25) to a grating spectrometer (Princeton Instruments Acton SP2500) with a CCD camera (Andor iKon-M). The cavity fiber is mounted on a three axis micropositioning mount. It can be withdrawn from the macroscopic mirror by some millimeters in order to use the setup as conventional confocal microscope.

Characterization. In a first step we characterize FNDs on Suprasil substrates replacing the macroscopic mirror with the fiber withdrawn. We confirm the presence of negatively charged NV centers by assessing fluorescence spectra, which show no significant contribution of NV^0 . We find that an appreciable fraction ($> 10\%$) of the fluorescent 12 nm diamonds contain single NVs by observing antibunching in the second order autocorrelation function of the photoluminescence. Comparing the average single emitter count rate with the fluorescence yield of 100 nm FNDs, we find that the latter host 30 – 300 NV centers per nanocrystal. For time resolved measurements we find fluorescence lifetimes ranging between 16 ns and 23 ns, a typical range for nanodiamonds.

Next we study FNDs prepared on a cavity mirror and with the fiber aligned to form a cavity. We perform

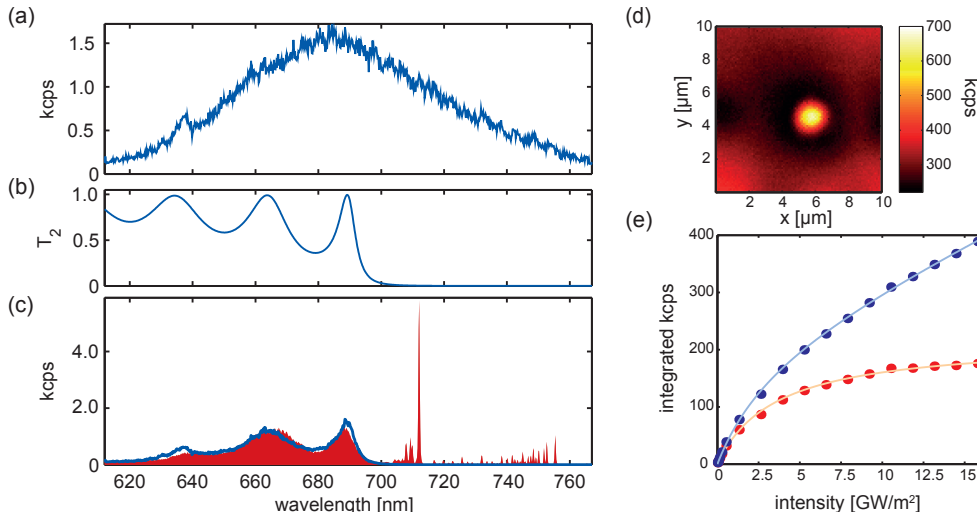


FIG. 2: (a) Free space spectrum of a 100 nm diamond on a Suprasil substrate (in units kilocounts per second). (b) Calculated transmission spectrum of the macroscopic mirror. (c) Emission spectrum of a FND placed inside the cavity. The transmissive part can be explained by the free space spectrum and the mirror transmission (blue line). Within the mirror stop band, cavity enhanced emission into narrow resonances is observed. (d) Confocal scan with $I = 0.5 I_{\text{sat}}$ showing a single nanodiamond, mirror background, and the effect of bleaching. (e) Saturation of free space NV emission (blue datapoints). Same measurement with linear background subtracted (red datapoints). Solid lines are fits to a saturation model.

confocal scans with the mirror surface facing the fiber and detect the partial transmission through the mirror as shown Fig. 2(d). We observe strong background fluorescence within the detection spectral band, originating from fluorescence generated in the mirror and the fiber, as well as from Raman scattering in the fiber. To obtain signals much stronger than the mirror background, we use 100 nm nanodiamonds containing ensembles of NV centers. With a coating that prevents excitation light from entering the fiber, excessive background is avoidable and also permits single emitter experiments [30].

For the measurements shown below, the observed fluorescence corresponds to ~ 50 NV centers originating from a diffraction-limited spot. With the respective FND positioned in the focus of the microscope objective, we align the fiber to form a cavity such that the fundamental mode has optimal overlap with the FND. Figure 2(c) shows a typical spectrum obtained under such conditions. To understand the different parts of the spectrum, we show a typical free space spectrum taken on a Suprasil substrate with negligible background [Fig. 2(a)] and a calculation of the mirror transmission $T_2(\lambda)$ [Fig. 2(b)]. Multiplying the two contributions and scaling with a constant matches the modulated emission observed under cavity conditions for the short wavelength part [Fig. 2(c)]. Within the stop band of the coating we observe enhanced emission into sharp cavity resonances. For the measurement shown, subsequent fundamental modes at $\lambda_1 = 715$ nm and $\lambda_2 = 755$ nm and a series of weak higher order transverse modes are visible. The separation of the fundamental modes gives direct access to the ef-

fective cavity length $d_{\text{eff}} = \lambda_1 \lambda_2 / [2(\lambda_2 - \lambda_1)] = 6.75 \mu\text{m}$. This length contains the part of the cavity mode penetrating into the mirror stack. From a simulation of the coating at the respective wavelengths we find that the penetration adds up to $1.5 \mu\text{m}$. Evaluating the separation of the higher order transverse modes $\Delta\lambda_{nm} = \lambda^2 \arccos(\sqrt{1 - d_{\text{eff}}/r}) / (2\pi d_{\text{eff}})$ we infer the effective radius of curvature of the fiber mirror, $r = 100 \mu\text{m}$, in agreement with white light interferometric measurements of the fiber surface. This determines the mode waist w_0 and volume V of the plane-concave cavity, given by $w_0^2 = \lambda / \pi \sqrt{r d_{\text{eff}} - d_{\text{eff}}^2}$ and $V = \pi w_0^2 d_{\text{eff}} / 4$, respectively. Since $d_{\text{eff}} \ll r$ and $w_0 \gg \lambda/2$, the paraxial approximation and thus the given formulas are valid to a high precision.

To characterize the background contribution, we retract the fiber and perform saturation measurements. We observe an intensity dependence that contains a saturating part and a linear contribution from background fluorescence, shown in Fig. 2(e). Fitting the integrated count rate of the transmissive part to the function $P = P_\infty I / (I_{\text{sat}} + I) + aI$, with the intensity I and the fitting parameters $P_\infty, I_{\text{sat}}, a$, we find a saturation intensity $I_{\text{sat}} = 3.5 \text{ GW/m}^2$ for the studied FND, which agrees with typical reported values [2], and a background contribution of 20% in the linear regime of the NV fluorescence. Within the mirror stopband and for the cavity present we find a signal to background ratio of about 100 for strong cavity resonances. Taken together, the spectrum, saturation, and lifetime measurements confirm that we are indeed coupling NV emission to the cavity.

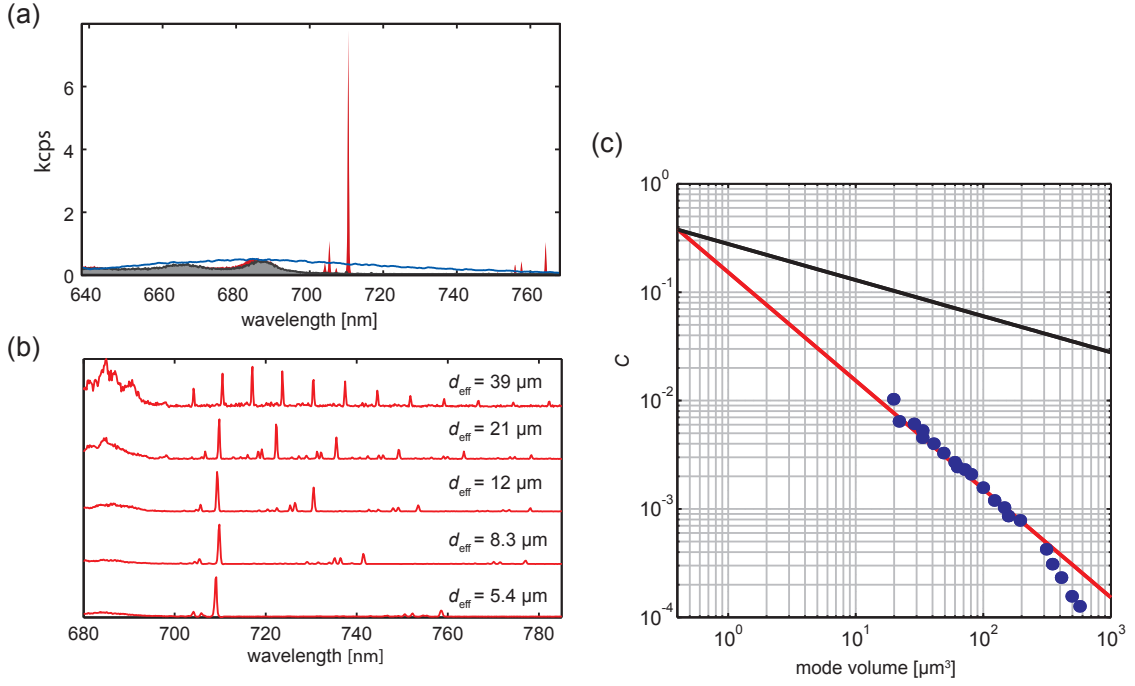


FIG. 3: (a) Comparison of the FND spectrum as inferred for free space conditions (S_{fs} , blue), emission through the mirror with the fiber retracted (S_m , gray), and for a cavity configuration with $d_{eff} = 5.0 \mu m$ (S_c , red). (b) Normalized spectra for decreasing cavity length from $d_{eff} = 39 \mu m$ (top) to $5.4 \mu m$ (bottom). (c) Scaling behavior of the Purcell enhancement in the bad emitter regime: Effective Purcell factor evaluated for the strongest cavity resonance at $\lambda_0 = 710$ nm as a function of mode volume (blue data points). The red line shows the prediction of Eq. (2), the black line shows the ideal Purcell factor as given by Eq. (1) divided by a factor 100 for easier comparison.

Effective Purcell Factor. The ideal Purcell factor C_0 describes the enhancement of the emission rate of an emitter whose entire fluorescence spectrum is coupled to an optical cavity resonance with quality factor $Q = \lambda_0/\delta\lambda$ and mode volume V ,

$$C_0 = \frac{3\lambda^3 Q}{4\pi^2 V}. \quad (1)$$

For the bad emitter regime, i.e. for broadband emitters with spectral width $\delta\lambda_{em}$ much larger than the full cavity linewidth $\delta\lambda$, only a fraction $\xi \approx \delta\lambda/\delta\lambda_{em}$ of the emission couples to the cavity. This reduces the Purcell factor to

$$C \approx \xi C_0 = \frac{3\lambda_0^3 Q_{em}}{4\pi^2 V}. \quad (2)$$

In this regime, the effective Purcell factor no longer depends on the quality factor of the cavity but rather on the quality factor of the emitter, $Q_{em} = \lambda_0/\delta\lambda_{em}$.

For a direct evaluation of the effective Purcell factor we compare spectra for three different configurations: A free space reference spectrum $S_0(\lambda)$ from a FND on a Suprasil substrate, and spectra $S_c(\lambda)$ and $S_m(\lambda)$ from the FND under study on the mirror inside and outside of the cavity respectively, where background is subtracted. We infer the free space emission spectrum $S_{fs}(\lambda) = bS_0(\lambda)$ of the FND under study from its emission spectrum obtained

through the mirror by matching $S_m(\lambda)$ to $bT_2(\lambda)S_0(\lambda)$ via the scaling factor b determined by a least square fit. Here, $T_2(\lambda)$ is the transmission of the macroscopic mirror which we infer from a direct transmission measurement and simulate with a transfer matrix method [37].

With this at hand we can compare the integrated emission into the strongest cavity resonance $P_c = \int_{\lambda_0-\Delta}^{\lambda_0+\Delta} S_c(\lambda)d\lambda$ with the integrated emission under free space conditions $P_{fs} = \int S_{fs}(\lambda)d\lambda$, where Δ denotes a suitable integration range around the resonance. The Purcell factor compares the emission rate into a particular cavity mode with the free space emission into the entire solid angle, such that one has to account for the probability for emitted photons to reach the detector for both cases. In the free space case, we only collect photons emitted into the solid angle of the objective $\Omega = 2\pi(1 - \cos\phi)$ with $\phi = \arcsin(\text{NA})$, which we account for by introducing a factor $4\pi/\Omega$. For a photon emitted into the cavity, we include the probability to leave the cavity through the respective mirror, $p(T_2) = T_2/(T_1 + T_2 + L_1 + L_2)$, where L_1 and L_2 is the loss of the fiber mirror and the macroscopic mirror respectively. At the wavelength of the cavity resonance, $\lambda_0 = 710$ nm, we obtain $p(T_2) = 0.68$, where we use the measured values $L_{1,2} = (71, 23)$ ppm, and $T_{1,2}(\lambda_0) = (810, 1900)$ ppm from the coating simulation.

Loss on the way to the detector and detector efficiency are assumed to be equal for free space and cavity conditions and thus cancel out. Furthermore, we estimate only a minor effect due to the fixed dipole orientations owing to ensemble averaging.

Overall, this yields an experimental value for the effective Purcell factor

$$C = \frac{P_c}{P_{fs}} \frac{\Omega}{4\pi} \frac{1}{p(T_2)}. \quad (3)$$

For the spectrum shown in Fig. 3 (a) we obtain a value $C = (1 \pm 0.2) \times 10^{-2}$. The error is dominated by the systematic uncertainty of our evaluation method. As expected for such a low value for C , we don't observe a change in the emission lifetime.

To obtain quantitative agreement between the prediction of Eq. (2) and our measurements evaluated according to Eq. (3), we include the electric field strength E at the position of the emitter compared to the field maximum E_m in a standing wave antinode. This reduces the coupling in particular close to the edge of the stop band of the mirror, where a phase shift results from the dispersive character of the coating. For the given resonance position and our coating parameters we calculate $(E/E_0)^2 = 0.55$, approaching unity for longer wavelengths. Evaluating Eq. (2) for the parameters of the measurement ($V = 19 \mu\text{m}^3, Q_{em} = 10$) we obtain $(E/E_0)C = (0.8 \pm 0.1) \times 10^{-2}$, in good agreement with the experimental value. To demonstrate the scaling of Eq. (2) explicitly, we perform measurements as shown in Fig. 3(a) and evaluate the effective Purcell factor for the emission into the strongest cavity resonance as a function of the cavity mode volume by changing the mirror separation. A few example spectra are shown in Figure 3(b), the evaluation of the full data set is shown in (c). The observed behavior matches the prediction of Eq. (2) very well, given the fact that no free parameters enter. Notably, C approaches unity only for very small mode volumes on the order of λ^3 . We expect that this regime can be approached with fiber-based Fabry-Perot cavities by further miniaturization.

Ideal Purcell Factor. In contrast to the small fraction of the entire emission that is coupled to the resonator, we observe a strong enhancement of the emission spectral density on cavity resonance. In fact, comparing the spectral density for the cavity and free space case quantifies the ideal Purcell factor C_0 . With the strong variation of our coating properties across the emission spectrum, we can furthermore study the enhancement as a function of the quality factor of the cavity. By changing the mirror separation we can locate the cavity resonance at any wavelength and thereby sample quality factors spanning a range of almost three orders of magnitude. Figure 4(a) shows the stepwise tuning of a cavity resonance across one free spectral range for a short mean cavity length $\langle d_{\text{eff}} \rangle = 4.5 \mu\text{m}$, corresponding to the mode with 8 antin-

odes between the mirrors. For comparison, we show a single spectrum for large cavity length $d_{\text{eff}} = 39 \mu\text{m}$ in Fig. 4(b), where the cavity geometry and the excitation conditions are fixed. There, several consecutive fundamental modes between 700 nm and 800 nm are observed within the mirror stop band, sampling different Q within a single measurement.

The ideal Purcell factor can now be evaluated by comparing the maximal spectral density on resonance $S_{c,\text{max}}(\lambda_0)$ with the free space value $S_{fs}(\lambda_0)$ at the same wavelength. Since the cavity linewidth is beyond the resolution of our spectrometer, we infer the peak spectral density of a Lorentzian resonance $S_{c,\text{max}} = 2P_c/\pi\delta\lambda$ and use the cavity linewidth $\delta\lambda = \lambda_0^2(T_1 + T_2 + L_1 + L_2)/4\pi d\sqrt{R_1 R_2}$, where $R_i = 1 - T_i - L_i$. For $\lambda_0 = 780 \text{ nm}$ we measure $Q = \lambda_0/\delta\lambda$ with a narrowband diode laser, while for low Q we use broadband light and the spectrometer. A calculation of $Q(\lambda)$ together with the measurements are shown in Fig. 4(d). The free space spectrum as well as corrections due to the collection efficiency and mirror loss are treated in analogy to the previous evaluation. Together, the ideal Purcell factor is determined experimentally by

$$C_0 = \frac{S_{c,\text{max}}}{S_{fs}} \frac{\Omega}{4\pi} \frac{1}{p(T_2)}. \quad (4)$$

In Fig. 4(c) the values obtained from the data sets partially shown in Fig. 4(a),(b) are compared with theory. Good agreement with Eq. 1 is achieved without free parameters if the calculated ideal Purcell factor again includes the wavelength dependence of the electric field strength at the position of the nanodiamond. For $d_{\text{eff}} = 4.3 \mu\text{m}$ and $Q = (3.5 \pm 0.3) \times 10^5$, the measurements yield a maximum value of $C_0 = 450 \pm 50$, one of the largest values reported to date. Notably, we observe only minor changes of the Finesse (or the quality factor) measured at the largest value when introducing the nanocrystal ($< 20\%$), which we explain by Purcell suppression of Rayleigh scattering loss [38, 39].

Rate model. In the previous sections we have approximated the NV emission by a single transition with large effective linewidth to simplify the discussion. A more accurate treatment accounts for the individual transitions making up the emission spectrum and the respective rates involved. The coupled system can therefore be described in the framework of the dissipative Jaynes Cummings theory including excessive dephasing [40, 41]. We consider the dynamics governed by the coherent coupling rate g_0 , the cavity decay rate κ , the decay rate of the emitter γ , and the excessive dephasing rate γ^* . Coupling to phonons distributes the dipole matrix element between the ZPL and individual sideband transitions. To simplify the description of the sideband, a single phonon mode picture is used, where the k -th phonon sideband is approximated by a Lorentzian with effective width γ_k^* and transition strength ζ_k . In this way we can treat the

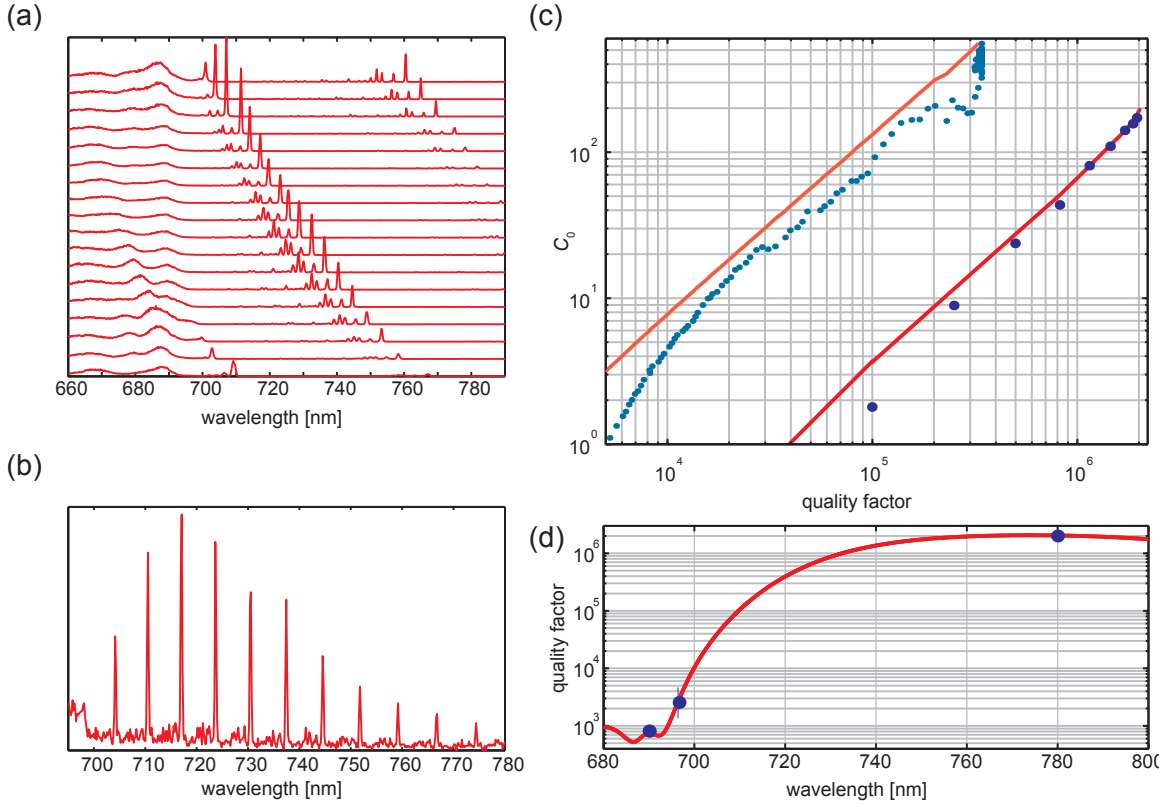


FIG. 4: (a) Tuning of a single cavity resonance across the accessible NV spectrum for $\langle d_{\text{eff}} \rangle = 4.5 \mu\text{m}$. (b) Cavity spectrum with multiple resonances for $d_{\text{eff}} = 39 \mu\text{m}$. (c) Ideal Purcell factor as a function of the quality factor for the data set partially shown in (a) (light blue) and (b) (dark blue) together with the predictions of Eq. (1) including the local field strength (solid lines). (d) Measurement (blue datapoints) and calculation (solid line) of the cavity quality factor as a function of the wavelength for $d_{\text{eff}} = 39 \mu\text{m}$.

ZPL ($k = 0$) and the sideband ($k = 1 \dots n$) in the same manner. The coupling rate for a single emitter and an individual transition is then given by

$$g_{0k} = \frac{\vec{\mu}_k \vec{E}_k}{\hbar} = \frac{E_k}{E_{0k}} \sqrt{\frac{3\pi^2 c^3}{2\omega_k^2 V}} \zeta_k \gamma \cos \theta, \quad (5)$$

where we have included the relative orientation $\cos \theta$ between the dipole of the NV and the electric field of the cavity mode, and the reduced electric field at the emitter compared to an antinode E_k/E_{0k} . Finally, the energy decay rate of the cavity at the respective transition frequency is given by $\kappa_k = c(T_1 + T_2 + L_1 + L_2)/2d_{\text{eff}}\sqrt{R_1 R_2}$ and $\gamma = 1/\tau = 2\pi \times 8 \text{ MHz}$ for typical nanodiamonds.

Generalizing the results from [40, 41] one finds that the effective coupling rate between the emitter and the cavity at resonance frequency ω_c is given by

$$R(\omega_c) = \sum_k \frac{4g_{0k}^2 \Gamma_k}{\Gamma_k^2 + 4\Delta_k^2}. \quad (6)$$

Here we account for all contributing transitions with respective frequencies ω_k , coupling strengths g_{0k} , total incoherent rates $\Gamma_k = \kappa_k + \gamma + \gamma_k^*$, and cavity detunings

$\Delta_k = \omega_c - \omega_k$. The effective Purcell factor is then given by $C(\omega_c) = R(\omega_c)/\gamma$. One can see that C becomes independent of κ_k for $\gamma_k^* \gg \kappa_k$, supporting the previous definition in Eq. (2).

We note that the coupling of a number of N emitters to the cavity does not lead to a change of the coupling rate in the present situation. This is in contrast to the case of a coherent ensemble, where a collective dipole forms that leads to an increased coupling rate $g_N = \sqrt{N}g_0$. Collective enhancement in the presence of strong dephasing can be quantified by the figure of merit $\alpha = NR/\gamma^*$, which compares the enhanced emission rate under ideal conditions with the dephasing rate [42]. While modification of the dynamics becomes apparent for $\alpha > 0.1$, we find $\alpha \sim 10^{-3}$ for our parameters, such that no collective effects are expected.

To model the measurements of our experiment, we fit ζ_k and γ_k^* with $\omega_k = 2\pi(469 - k \times 16) \text{ THz}$ to reproduce the free space spectrum $S_0(\omega)$ and determine all other quantities from measurements. We find $\zeta_k = [0.02, 0.25, 0.44, 0.24, 0.06, 0.01]$, $\gamma_k^* = [3.1, 23, 25, 29, 34, 40] \text{ THz}$, contribution of transitions with larger k are negligible. We find good agreement

between the predictions of the model and the data, e.g. for the parameters of the measurement shown in Fig. 3(a) we obtain $C = 1.0 \times 10^{-2}$.

This generalized description of cavity enhancement confirms that the simple picture given previously is a sufficient approximation as long as the effective dephasing dominates all other rates and masks the structure of the phonon sideband. Beyond this, the model provides insight into the different roles of transition branching and dephasing.

Conclusion and Outlook. In our experiment we have studied the scaling laws for the cavity enhancement of the fluorescence of broadband emitters with a flexible architecture, offering high Finesse and large ideal Purcell factors compatible with the presence of nanodiamonds. The results indicate a way for the realization of efficient single-photon sources with narrow bandwidth and wide tunability, and suggest that fiber-based micro cavities could provide a route towards the strong coupling regime in a cryogenic environment.

While NV centers in nanocrystals show larger homogeneous linewidth and stronger spectral diffusion than in clean bulk samples, dephasing rates $\gamma^*/2\pi < 500$ MHz for the ZPL appear feasible. Alternatively, diamond membranes or nanomachined high quality bulk diamond could be introduced to achieve better optical and spin properties. For an estimation of the achievable coupling strength we account for the ZPL branching ratio $\zeta_0 = 0.04$ and the splitting of the ZPL into six individual fine structure resonances. For the transitions connecting the $m_S = 0$ ground state with the E_x or E_y levels in the excited state, an overall branching ratio $\zeta_0(E_x, E_y) \approx 0.02$ remains for perfect state initialization [43]. Optimization of the laser machining technique is expected to achieve mirror radii of curvature $< 10 \mu\text{m}$, which would result in $g_{00} > 1$ GHz for $d_{\text{eff}} = 2.0 \mu\text{m}$. Applying a feasible coating with $T + L = 20$ ppm at 637 nm yields $\mathcal{F} = 150000$ and $\kappa/2\pi = 500$ MHz at this mirror separation. Together, this would reach the strong coupling regime, $2g_{00} > (\kappa, \gamma, \gamma^*)$, and lead to an effective Purcell Factor $C > 400$. This opens the perspective for a fully quantum-coherent spin-photon interface.

We acknowledge support from L. Costa, M. Mader, M. Weber, L. Liebermeister, and D. Burchardt, and helpful discussions with R. Albrecht, C. Becher, and A. Kubanek. This work was supported by the Nanosystems Initiative Munich. T.W.H. gratefully acknowledges support by the Max-Planck-Foundation.

* To whom correspondence should be addressed. E-mail: david.hunger@physik.lmu.de

[1] A. Gruber, A. Drabenstedt, C. Tietz, L. Fleury, J. Wrachtrup, and C. Borczyskowski, *Science* **276**, 2012 (1997).

- [2] C. Kurtsiefer, S. Mayer, P. Zarda, and H. Weinfurter, *Phys. Rev. Lett.* **85**, 290 (2000).
- [3] G. Balasubramanian, P. Neumann, D. Twitchen, M. Markham, R. Kolesov, N. Mizuochi, J. Achard, J. Beck, J. Tissler, V. Jacques, et al., *Nature Materials* **8**, 383 (2009).
- [4] P. C. Maurer, G. Kucsko, C. Latta, L. Jiang, N. Y. Yao, S. D. Bennett, F. Pastawski, D. Hunger, N. Chisholm, M. Markham, et al., *Science* **336**, 1283 (2012).
- [5] C.-H. Su, A. D. Greentree, and L. C. L. Hollenberg, *Optics Express* **16**, 6240 (2008).
- [6] A. Young, C. Y. Hu, L. Marseglia, J. P. Harrison, J. L. O'Brien, and J. G. Rarity, *New J. of Phys.* **11**, 013007 (2009).
- [7] L. Robledo, L. Childress, H. Bernien, B. Hensen, P. Alkemade, and R. Hanson, *Nature* **477**, 574 (2011).
- [8] E. Togan, Y. Chu, A. S. Trifonov, L. Jiang, J. Maze, L. Childress, M. V. G. Dutt, A. S. Sorensen, P. R. Hemmer, A. S. Zibrov, et al., *Nature* **466**, 730 (2010).
- [9] J. Wolters, A. W. Schell, G. Kewes, N. Nüsse, M. Schönggen, H. Döscher, T. Hannappel, B. Löchel, M. Barth, and O. Benson, *Appl. Phys. Lett.* **97**, 141108 (2010).
- [10] D. Englund, B. Shields, K. Rivoire, F. Hatami, J. Vučković, H. Park, and M. D. Lukin, *Nano Letters* **10**, 3922 (2010).
- [11] T. van der Sar, J. Hagemeyer, W. Pfaff, E. C. Heeres, S. M. Thon, H. Kim, P. M. Pietroff, T. H. Oosterkamp, D. Bouwmeester, and R. Hanson, *Appl. Phys. Lett.* **98**, 193103 (2011).
- [12] J. Riedrich-Möller, L. Kipfstuhl, C. Hepp, E. Neu, C. Pauly, F. Mücklich, A. Baur, M. Wandt, S. Wolff, M. Fischer, et al., *Nature Nanotechnology* **7**, 69 (2012).
- [13] A. Faraon, C. Santori, Z. Huang, V. M. Acosta, and R. G. Beausoleil, *Phys. Rev. Lett.* **109**, 033604 (2012).
- [14] A. Faraon, P. E. Barclay, C. Santori, K.-M. C. Fu, and R. G. Beausoleil, *Nature Photonics* **5**, 301 (2011).
- [15] B. Hausmann, B. Shields, Q. Quan, P. Maletinsky, M. McCutcheon, J. T. Choy, T. M. Babinec, A. Kubanek, A. Yacoby, M. D. Lukin, et al., *Nano Letters* **12**, 1578 (2012).
- [16] P. E. Barclay, K.-M. Fu, C. Santori, and R. G. Beausoleil, *Appl. Phys. Lett.* **95**, 191115 (2009).
- [17] P. E. Barclay, C. Santori, K.-M. C. Fu, R. G. Beausoleil, and O. Painter, *Optics Express* **10**, 8081 (2009).
- [18] Y. Dumeige, R. Allaupe, P. Grangier, F. Treussart, and J.-F. Roch, *New J. of Phys.* **13**, 025015 (2011).
- [19] N. P. de Leon, B. J. Shields, C. L. Yu, D. E. Englund, A. V. Akimov, M. D. Lukin, and H. Park, *Phys. Rev. Lett.* **108**, 226803 (2012).
- [20] J. T. Choy, B. J. M. Hausmann, T. M. Babinec, I. Bulu, M. Khan, P. Maletinsky, A. Yacoby, and M. Loncar, *Nature Photonics* **5**, 738 (2011).
- [21] D. Hunger, T. Steinmetz, Y. Colombe, C. Deutsch, T. W. Hänsch, and J. Reichel, *New J. Phys.* **12**, 065038 (2010).
- [22] D. Hunger, C. Deutsch, R. J. Barbour, R. J. Warburton, and J. Reichel, *AIP Advances* **2**, 012119 (2012).
- [23] Y. Colombe, T. Steinmetz, G. Dubois, F. Linke, D. Hunger, and J. Reichel, *Nature* **450**, 272 (2007).
- [24] M. Steiner, H. M. Meyer, C. Deutsch, J. Reichel, and M. Köhl, *Phys. Rev. Lett.* **110**, 043003 (2013).
- [25] C. Toninelli, Y. Delley, T. Stöferle, A. Renn, S. Götzinger, and V. Sandoghdar, *Appl. Phys. Lett.* **97**, 021107 (2010).
- [26] A. Muller, E. B. Flagg, M. Metcalfe, J. Lawall, and G. S.

- Solomon, *Appl. Phys. Lett.* **95**, 173101 (2009).
- [27] R. J. Barbour, P. A. Dalgarno, A. Curran, K. M. Nowak, H. J. Baker, D. R. Hall, N. G. Stoltz, P. M. Petroff, and R. J. Warburton, *J. Appl. Phys.* **110**, 053107 (2011).
- [28] Z. Di, H. V. Jones, P. R. Dolan, S. M. Fairclough, M. B. Wincott, J. Fill, G. M. Hughes, and J. M. Smith, *New J. of Phys.* **14**, 103048 (2012).
- [29] J. Miguel-Sánchez, A. Reinhard, E. Togan, T. Volz, A. Imamoğlu, B. Bresga, J. Reichel, and J. Estève, *arXiv:1211.4515* (2013).
- [30] R. Albrecht, A. Bommer, C. Deutsch, J. Reichel, and C. Becher, *arXiv:1303.7418* (2013).
- [31] N. Mohan, Y.-K. Tzeng, L. Yang, Y.-Y. Chen, Y. Y. Hui, C. Y. Fang, and H. C. Chang, *Adv. Mater.* **22**, 843 (2010).
- [32] S.-J. Yu, M. W. Kang, H.-C. Chang, K.-M. Chen, and Y.-C. Yu, *J. Am. Chem. Soc.* **127**, 17604 (2005).
- [33] L. Rondin, G. Dantelle, A. Slablab, F. Treussart, P. Bergonzo, S. Perruchas, T. Gacoin, M. Chaigneau, H.-C. Chang, et al., *Phys. Rev. B* **82**, 115449 (2010).
- [34] M. V. Hauf, B. Grotz, B. Naydenov, M. Dankerl, S. Pezzagna, J. Meijer, F. Jelezko, J. Wrachtrup, M. Stutzmann, F. Reinhard, et al., *Phys. Rev. B* **83**, 081304(R) (2011).
- [35] K.-M. C. Fu, C. Santori, P.-E. Barclay, L.-J. Rogers, N.-B. Manson, and R.-G. Beausoleil, *Phys. Rev. Lett.* **103**, 256404 (2009).
- [36] G. Davies, *J. Phys. C: Solid State Phys.* **7**, 3797 (1974).
- [37] C. J. Hood, H. J. Kimble, and J. Ye, *Phys. Rev. A* **64**, 033804 (2001).
- [38] M. Motsch, M. Zeppenfeld, P. W. H. Pinkse, and G. Rempe, *New J. of Phys.* **12**, 063022 (2010).
- [39] T. J. Kippenberg, A. L. Tchebotareva, J. Kalkman, A. Polman, and K. J. Vahala, *Phys. Rev. Lett.* **103**, 027406 (2009).
- [40] A. Auffèves, D. Gerace, J.-M. Gérard, M. F. Santos, L. C. Andreani, and J.-P. Poizat, *Phys. Rev. B* **81**, 245419 (2010).
- [41] E. del Valle and F. P. Laussy, *Phys. Rev. A* **84**, 043816 (2011).
- [42] V. V. Temnov and U. Woggon, *Phys. Rev. Lett.* **95**, 243602 (2005).
- [43] N. B. Manson, J. P. Harrison, and M. J. Sellars, *Phys. Rev. B* **74**, 104303 (2006).